A Closer Look at Linear Stability Theory in Modeling Spray Atomization

Arpit Agarwal[a], Mario F. Trujillo[a]

[a]*Department of Mechanical Engineering, University of Wisconsin-Madison, Madison, WI 53706, USA*

Abstract

The common Lagrangian-Eulerian modeling of liquid sprays is largely based on linear stability theory, where the associated growth rates and most unstable wavelengths are used in prescribing initial Lagrangian droplet characteristics. Using highly-resolved VoF simulations, the present work is aimed at examining the extent to which this linear stability and associated flow characteristics hold in a realistic spray configuration under normal operating conditions using the ECN spray A geometry. This involves a comparison between linear stability wavelength predictions, originating from two-phase Orr-Sommerfeld solutions, and those obtained from the VoF simulations. The results show that within the first 4 diameters beyond the orifice, the non-linear components of the Navier-Stokes have grown to 10% of the corresponding linear part in both the liquid and the gas phase, and continue to grow exponentially. The non-axial and non-fully developed flow profiles are particularly significant even within one diameter but do not develop as strongly as the non-linear components. Linear stability theory is able to adequately capture the initial surface disturbances, and there is reasonable agreement with VoF simulations, despite the fact that the base flow is not exactly the conventional one. A main finding from the work shows that while the most unstable modes are captured in the simulations and agree with theoretical predictions, these modes are *not* directly responsible for fragmenting the liquid core or causing primary atomization. Their action is limited to breaking up the surface of the jet, while the liquid core of the jet remains intact for another 20 jet diameters downstream.

Keywords: Primary Atomization; Linear Stability Theory; Breakup Models.

1. Introduction

Primary atomization in sprays, defined as the complete fragmentation of a liquid jet, has been the subject of a large number of research efforts [1–3] due in part to its practical relevance in fuel injection [4]. Apart from some recent DNS-type studies [5–11] that resolve and sharply capture the liquid-gas interface at a high computational expense, the vast majority of atomization calculations have relied on models to describe relevant physics. Under this modeling approach, the computational expense is significantly reduced, but the atomization process is completely under-resolved, which puts a heavy reliance on the performance of spray breakup models. Commonly, these breakup models are combined with a Lagrangian-Eulerian description of the resulting spray, and this approach has dominated spray modeling for the last 20-30 years [12–19]. In fact, it currently has been incorporated into commercial engine CFD codes including CONVERGE CFD, ANSYS-FORTE, STAR-CD, and AVL-FIRE.

A common procedure for developing breakup models is based on linear stability theory [20, 21] along with corresponding atomization models, which dictate how the most unstable modes transition into droplets. As documented in the literature [22, 23], it is well established that linear theory has achieved success in predicting the most unstable modes in various canonical two-phase flows, such as liquid sheets, cylindrical jets, annular jets, liquid films, and liquid threads. For these flows, the initial configuration and identification of the base state is well characterized and often the associated flows are completely laminar. However, even for cases having higher Reynolds number the predictions from instability theory have been found to agree well with experiments and highly-resolved simulations. A notable example is the study by Fuster et al. [24] concerning co-flowing sheets, where the predictions of the most unstable frequency generated from linear theory agree relatively well with experiments in addition to predicting correctly the transition from convective to absolute instability.

Perhaps, motivated by the success of linear theory in predicting various breakup phenomena, it has been used as a fundamental tool for the development of breakup models for sprays occurring at much larger Reynolds numbers and influenced by more complicated physics [20, 21]. In particular in automotive sprays, e.g. Diesel sprays, the liquid based Reynolds number is generally $\mathcal{O}(10^4) - \mathcal{O}(10^5)$ putting the jet breakup phenomena well into the turbulent and full atomization regimes [25]. Also, the nozzles are often well below 1 mm in diameter, which implies that the internal wall surface imperfections and roughness play an important role in conditioning the flow prior to its exit.

Under certain conditions, the pressure environment is such that cavitation occurs within the nozzle further complicating the physics. Nevertheless, in spite of these complications, the breakup models have achieved relatively good agreement with experiments provided the modeling constants are well calibrated. In view of the complications associated with realistic spray configurations, a closer look at the underlying characteristics in regards to the linear stability theory is warranted. This closer look is provided in the present work using highly-resolved simulations based on a Volume-of-Fluid (VoF) methodology. In this spirit the present work aims to accomplish the following three goals.

First, we are interested in investigating the extent of the validity of the underlying linear stability assumptions. Explicitly, in a linearized analysis of liquid injection, the velocity perturbations are assumed to be small, the base velocity is assumed to be completely axial and fully developed, and the liquid surface is described by a superposition of sinusoidal modes. The second goal is estimating whether the most unstable modes originating from the linear regime and calculated via Orr-Sommerfeld agree with the more detailed VoF simulations. And for the third goal, it is examined whether these most violent perturbations are actually responsible for the fragmentation of the jet. This is a more fundamental question, since depending on the results, it can confirm or call to question the applicability of existing approaches for modeling breakup or atomization. To accurately capture the effects of nozzle imperfections and surface roughness, the Engine Combustion Network's[1] (ECN) Spray A nozzle configuration is employed with a fine, boundary-fitted grid. This is in contrast to external-only simulations [5–8, 10] and simulations with idealistic inflow conditions [11].

The paper is organized as follows. In Section 2, a description of the VoF methodology employed is given along with a presentation of the injector nozzle geometry. The computational methodology is validated in Section 3 against X-ray radiography measurements. In Section 4, the derivation of the linearized system that forms the basis of the breakup models is summarized and the assumptions in the theory are formally introduced. The results are then presented in Section 5 beginning with the analysis of the extent of the linear region, the comparison of linear stability theory with VoF simulations, and the implications for primary atomization. The findings of the work and final thoughts are discussed in Section 6.

[1] `https://ecn.sandia.gov/`

2. Description of Numerical Method and Jet Configuration

2.1. Computational Method

The VoF simulations reported in this paper are performed with an algebraic solver, `interFoam`, which forms a part of a larger open-source distribution of computational mechanics solvers and C++ libraries of OpenFOAM®[2]. The solver is based on a finite volume discretization on collocated grids for the solution of two-phase incompressible flows. A thorough evaluation of solver performance with respect to a broad range of two-phase flows is reported in our previous publication [26]. The evaluation was based on the performance with respect to kinematics of advection, dynamics in inertia dominated regime, and dynamics in the surface tension dominated regime. An abbreviated description is provided here; a more detailed explanation can be found in Ref. [26].

The first part of the solution consists of advecting the liquid fraction field, α, by solving the following conservation equation,

$$\frac{\partial \alpha}{\partial t} + \nabla \cdot (\tilde{\mathbf{U}}\alpha) = 0, \tag{1}$$

where $\tilde{\mathbf{U}}$ is the velocity field. The liquid fraction represents the volume fraction of liquid occupying a given computational cell, Ω_i, $i \in [1, N_{cells}]$. The discrete version of this equation is

$$\frac{\alpha^{n+1} - \alpha^n}{\Delta t} + \frac{1}{|\Omega_i|} \sum_{f \in \partial\Omega_i} (F_u + \lambda_M F_c) = 0, \tag{2}$$

where the fluxes are defined as

$$F_u = \phi_f^n \alpha_{f,\text{upwind}}^n \quad \text{and} \quad F_c = \phi_f^n \alpha_f^n + \phi_{rf}^n \alpha_{rf}^n (1 - \alpha_{rf}^n) - F_u. \tag{3}$$

Here n denotes time level, subscript f refers to a cell-face quantity, $\phi_f^n = \tilde{\mathbf{U}}_f^n \cdot \mathbf{S}_f$, and $\mathbf{S}_f$ is the outward normal vector corresponding to a given cell (not normalized). Since velocity (as well as α) are cell-centered quantities, $\tilde{\mathbf{U}}_f^n$ is obtained by weighted-averaging from cells sharing the given face. In the flux term, F_u, the upwind value for the liquid fraction is denoted by $\alpha_{f,\text{upwind}}^n$. With respect to F_c, α_f^n is determined from the second order vanLeer scheme [27]. The remaining quantities represent the compressive flux, i.e. $\phi_{rf}^n \alpha_{rf}^n (1 - \alpha_{rf}^n)$, where

$$\phi_{rf}^n = \min_{f' \in \Omega_i} \left(\frac{|\phi_{f'}^n|}{|\mathbf{S}_{f'}|}, \tilde{U}_{rf,\max} \right) (\mathbf{n}_f \cdot \mathbf{S}_f), \quad \text{and} \quad \tilde{U}_{rf,\max} = \max_{f \in \Omega} \left[\frac{|\phi_f^n|}{|\mathbf{S}_f|} \right]. \tag{4}$$

This compressive flux is used to mitigate the effects of numerical diffusion that would occur as a

[2] `http://www.openfoam.com`

result of the sharp gradients in α in the interfacial region. Lastly, the variable α_{rf}^{n} is obtained using the `interfaceCompression` scheme native to OpenFOAM [26, 28]. In numerical tests concerning the advection of a discontinuous profile, such as the α field, the treatment given above performs noticeably better than TVD schemes with regards to the preservation of the sharpness of the discontinuity.

With respect to momentum, the following equation is solved

$$\frac{\partial \rho \tilde{\mathbf{U}}}{\partial t} + \nabla \cdot (\rho \tilde{\mathbf{U}} \otimes \tilde{\mathbf{U}}) = -\nabla p_d + \Big[\nabla \cdot (\mu \nabla \tilde{\mathbf{U}}) + \nabla \tilde{\mathbf{U}} \cdot \nabla \mu\Big] - \mathbf{g} \cdot \mathbf{x} \nabla \rho + \int_{\Gamma(t)} \sigma \kappa \delta(\mathbf{x} - \mathbf{x}_s) \mathbf{n} d\Gamma(\mathbf{x}_s), \tag{5}$$

where the surface tension coefficient is given by σ, local curvature by κ, the gas-liquid interface by $\Gamma(t)$, the 3D Dirac Delta function by $\delta(\mathbf{x} - \mathbf{x}_s)$, and $\mathbf{x}_s$ is the integration variable over $\Gamma(t)$. The Continuum Surface Tension model [29] is employed, namely

$$\int_{\Gamma \cap \Omega_i} \sigma \kappa \delta(\mathbf{x} - \mathbf{x}_s) \mathbf{n} d\Gamma(\mathbf{x}_s) = \int_{\Omega_i} \sigma \kappa \nabla \alpha dV. \tag{6}$$

In the predictor step, the density and viscosity fields are regularized according to

$$\rho = \rho_l \alpha + \rho_g (1 - \alpha) \quad \text{and} \quad \mu = \mu_l \alpha + \mu_g (1 - \alpha). \tag{7}$$

The solution of the momentum equation is obtained via a PISO [30] iteration procedure. A predictor velocity is first constructed and then corrected to ensure momentum balance and mass continuity. Explicit formulation of the predictor velocity is a two step process, where first the viscous, advective and temporal terms in the momentum equation are used to generate a cell centered vector field, which is then projected to cell faces using a second order scheme. Contributions from surface tension and gravity terms are then added, concluding the predictor formulation. This procedure enforces a consistent discretization of surface tension and pressure gradient [26, 31].

Within the correction procedure, the pressure contribution is added to the flux of predictor velocity, and mass conservation is invoked to yield a Poisson equation for pressure. The linear system is then solved using a Preconditioned Conjugate Gradient method, with Diagonal Incomplete Cholesky as the preconditioner. In the present work we have used three PISO steps to arrive at predictions for $(\tilde{\mathbf{U}}^{n+1}, pd^{n+1})$.

2.2. Injector Nozzle Geometry

A single-hole, 90 μm diameter, Bosch injector named Spray A by the Engine Combustion Network[3] (ECN) collaboration, is used for the present study as it has been characterized extensively [32, 33], particularly in the near field. In the present work, the nozzle surface file[4] provided by Georgia Institute of Technology for the ECN Spray A nozzle (serial# 210675) has been used for generating the computational grid. This surface file is a spline-reconstructed dataset based on X-ray tomography measurements, which effectively removes surface roughness effects and artificial measurement fluctuations, but retains surface features that are noticeably larger than 3 μm. The nozzle geometry including details of its asymmetry and nozzle alignment are displayed in Fig. 1. The surface file clearly reveals the offset of the nozzle hole from the sac centerline (dashed line). Additionally, the inlet turning angles, for instance θ_1 and θ_2 are not the same [32], and the diameter of the nozzle hole decreases along the streamwise direction.

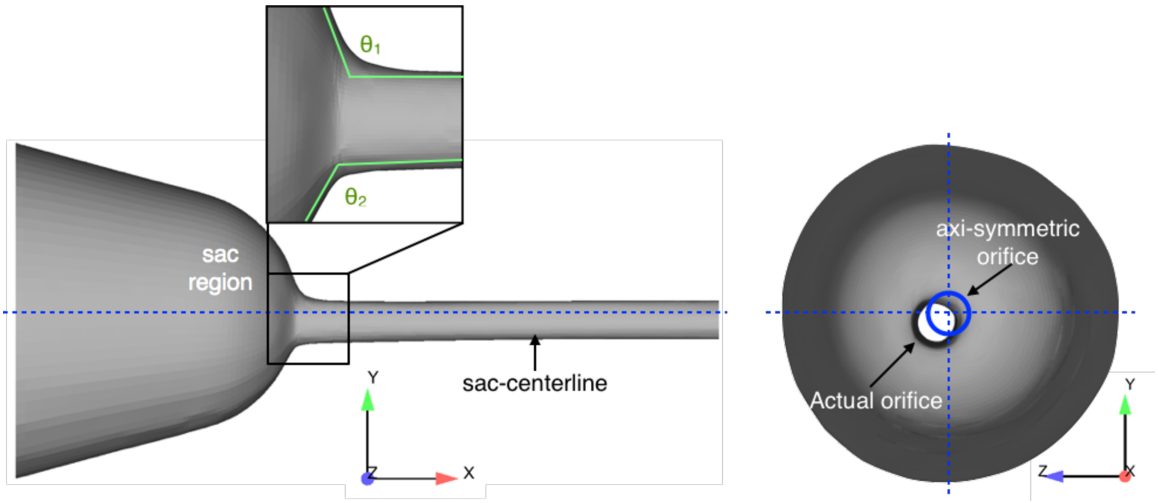

Figure 1: Asymmetries of the ECN SprayA nozzle are depicted. The actual alignment of the orifice superimposed on the axi-symmetric location is displayed. The dashed lined highlights the offset between the sac and the nozzle conduit. The variation in internal turning angles is emphasized in the inset where $\theta_1 \not\equiv \theta_2$.

2.3. Simulation Setup

Details of the computational domain are shown in Fig. 2. For the internal flow region, the grid boundaries coincide with the surface file for the nozzle and more importantly the surface imperfections are included in the numerical grid. This implies that their effect is captured in the simulations.

[3] https://ecn.sandia.gov/
[4] https://ecn.sandia.gov/diesel-spray-combustion/computational-method/meshes/

Three different grid levels have been employed in this study, with the mean grid size in the spray region having a respective value of $\Delta x = \{5.9\,\mu\text{m}, 3.9\,\mu\text{m}, 2.8\,\mu\text{m}\}$. There are 20, 31, and 40 cells across the nozzle for the coarsest, medium, and finest grids, respectively. The corresponding size distribution is displayed in Fig. 4 and shows that the cell sizes are closely distributed around their respective mean values. In this part of the domain all computational cells are hexahedral. Away from the spray region, in the farfield domain, unstructured cells are employed having much larger size as illustrated in Fig. 2a. In all calculations presented, the x coordinate is aligned with the jet axis and the origin is placed at the centroid of the orifice opening. The y axis is aligned with the transverse direction and the z axis is aligned with the spanwise direction as depicted in Fig. 2. Additionally, in Fig. 3, a representative result from the simulation is displayed showing the first 40 diameters from the injector nozzle.

For this study, all simulations have been performed at experimental conditions reported in [33], which adhere to the ECN specifications[5]. The ambient gas is N_2 at 343 K, and the fuel is n-dodecane at 303 K. Under these conditions and for the convergent nozzle geometry of the ECN Spray A case, vaporization and/or cavitation is not present [32, 34, 35]. Table 1 summarizes the fluid and flow properties used, and Table 2 presents the respective values of the key non-dimensional quantities. In the present simulations the inlet flow velocity (upstream of the nozzle) is specified such that the jet velocity at the orifice opening is 412 m/s to match the experimentally measured value [33].

ρ_l (kg/m^3)	ρ_g (kg/m^3)	ν_l (m^2/s)	ν_g (m^2/s)	σ (N/m)	U_{inj} (m/s)
715	22.8	1.007×10^{-6}	1.79×10^{-5}	0.021	412

Table 1: Fluid properties.

Re_l $(U_{inj}D/\nu_l)$	We_l $(\rho_l U_{inj}^2 D/\sigma)$	Oh_l $(We_l^{1/2}/Re_l)$	ρ_l/ρ_g ...
36,822	5.2×10^5	1.9×10^{-2}	31.36

Table 2: Values for relevant non-dimensional quantities.

[5] https://ecn.sandia.gov/diesel-spray-combustion/target-condition/spray-ab/

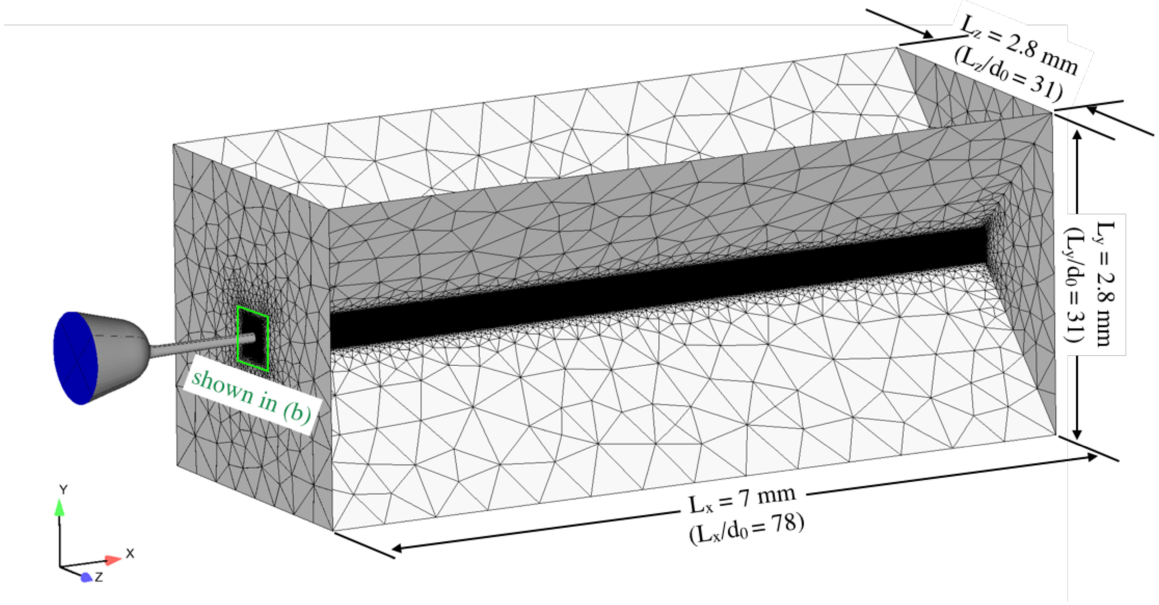

(a)

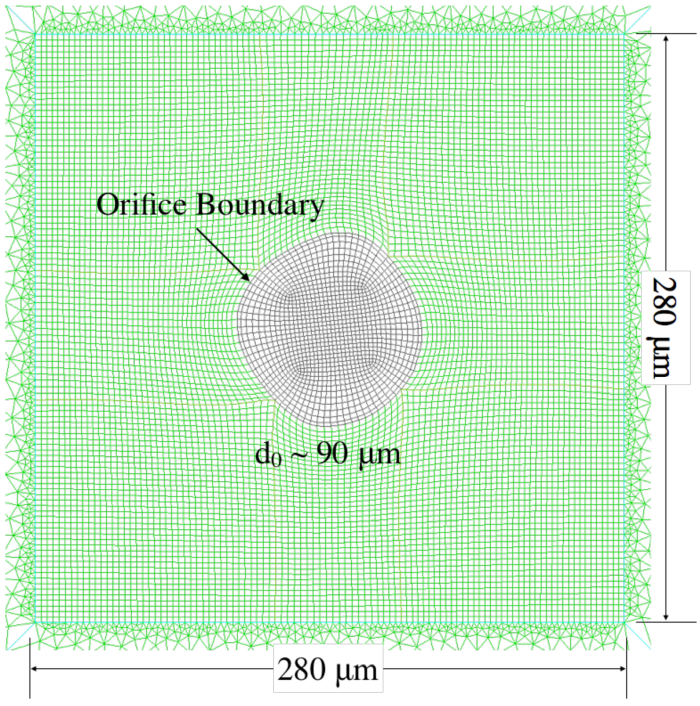

(b)

Figure 2: A visualization of the entire domain and grid is shown in (a) with the nozzle included on the left. The plane coinciding with the nozzle orifice is shown in (b), clearly portraying the asymmetry of the orifice.

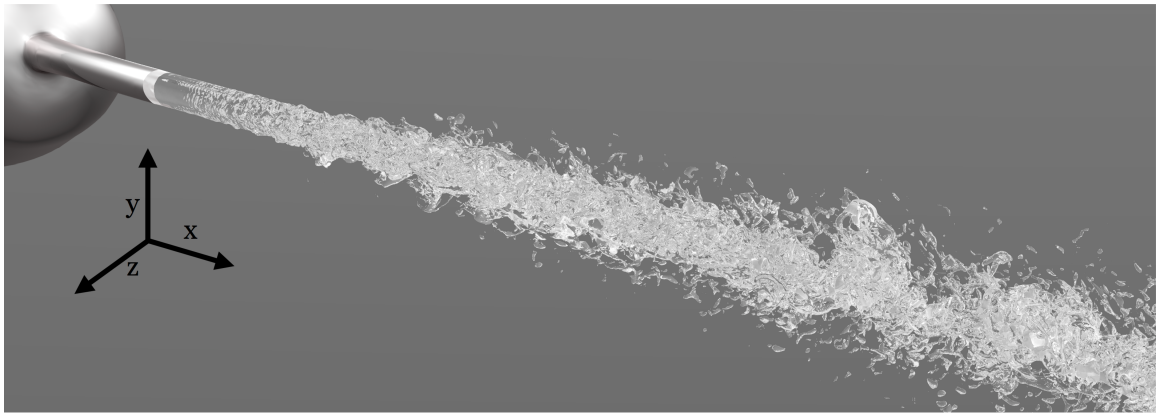

Figure 3: Visualization of the jet atomization for a typical simulation using the Spray A geometry.

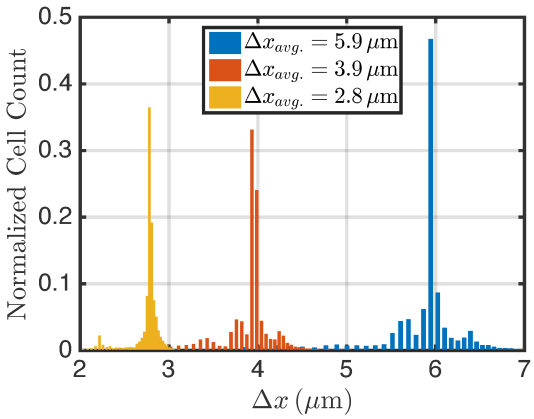

Figure 4: Distribution of cell sizes in the spray region for the three grids employed in the present study.

3. Validation

Performance of the `interFoam` solver employed in this study has been extensively evaluated [26] for a variety of two-phase problems, and validation tests have been presented for two-phase mixing layers and co-flow atomization [10]. Here, we present an additional test case where line integrated and time-averaged quantities are compared to experimental data. This provides a reasonable estimate of the behavior of the code in the near-field region. The configuration consists of the ECN Spray A case, as previously described. The metric for comparison is the Projected Mass Density (PMD), which is denoted as Φ. PMD is the line integrated liquid mass, and represents the projection of the 3D liquid mass distribution on a 2D plane. PMD computed along the y and z axes is respectively

given by

$$\Phi_y(x,z) = \rho_l \int_{-\infty}^{\infty} \langle \alpha(x,y,z) \rangle \, \mathrm{d}y, \tag{8a}$$

$$\Phi_z(x,y) = \rho_l \int_{-\infty}^{\infty} \langle \alpha(x,y,z) \rangle \, \mathrm{d}z. \tag{8b}$$

All computational data is reported in the form of temporally-averaged values, recognizing the fact that beyond the initial transient the process is statistically stationary. The time integration for relevant quantities, e.g. α, is given by

$$\langle \alpha(x,y,z) \rangle = \frac{1}{t_f - t_i} \int_{t_i}^{t_f} \alpha(x,y,z,t) \, \mathrm{d}t, \tag{9}$$

where $t_i = 25\,\mu$s and $t_f = 50\,\mu$s to ensure statistical convergence.

Quantitative comparisons of computed PMD against streamline centerline experimental [36] and transverse [33] measurements are presented. The centerline comparison is shown in Fig. 5, where the level of agreement for the finer grids is appreciably better than the coarse grid case (Δx=5.9 μm). To quantify the discrepancy, the mean relative error, $\mathcal{E}_\Phi$, defined as

$$\mathcal{E}_\Phi = \frac{1}{N} \sum_{i=1}^{N} \frac{|\Phi_{num,i} - \Phi_{exp,i}|}{\Phi_{exp,x=0}}, \tag{10}$$

is reported in Table 3. Here the subscript 'num' and 'exp' refer to numerical and experimental values, respectively, and N is the total number of data points.

For Φ_z, shown in Fig. 5a, computational results for the finer grids ($\Delta x = 3.9\,\mu$m and $2.8\,\mu$m) have an associated error below 5% for both cases. The error for the coarser case ($\Delta x = 5.9\,\mu$m) is higher at around 10%. Due to the expected spray asymmetry, as discussed in experimental findings [33], $\Phi_y \neq \Phi_z$, and while the trends in Φ_y (Fig. 5b) are similar to those in Φ_z (Fig. 5a), the values are different. This discrepancy between Φ_y and Φ_z peaks for the $\Delta x = 5.9\,\mu$m case between $x = 0.5$ mm and 3 mm.

To inspect the radial distribution of mass at different axial locations, Fig. 6 presents Φ_z profiles as a function of the y coordinate. As noted in Section 2.2, the spray axis is offset from the injector axis [32]. To correct for this offset the experimental spray axis has been aligned with the measured peak in the comparisons shown. Even though, Φ_y, is not provided for the sake of keeping the paper relatively short, the level of agreement with experiments is very similar to that of Φ_z.

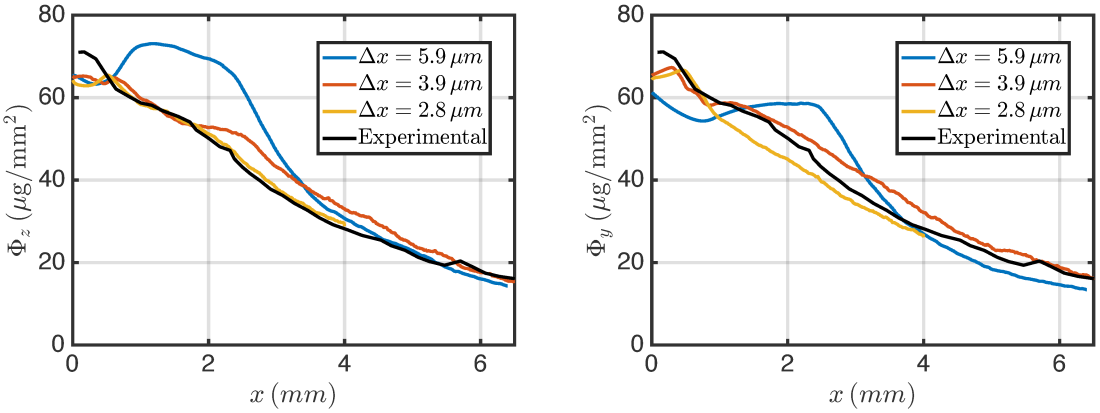

Figure 5: PMD along centerline for two different projection axes: (a) projection along z direction, (b) projection along y direction.

At $x = 0.1\,\mathrm{mm}$, the liquid jet is nearly intact with some small surface perturbations. As there is little or no atomization at this location, liquid is absent away from the jet. This mass distribution is reflected in Fig. 6a by a sharp rise in Φ_z along the centerline region. The computational data agrees well with the experimental data for the three grid levels at this location.

As we move downstream to $x = 2\,\mathrm{mm}$, the profiles are shown in Fig. 6b. Obviously, the coarse grid case, corresponding to $\Delta x = 5.9\,\mu\mathrm{m}$, shows poor agreement with measurements as opposed to the finer cases. This was observed in the centerline profiles as well. At this location, droplets and ligaments are present producing a smoother distribution for Φ_z. At $x = 4\,\mathrm{mm}$, primary atomization has already occurred and the jet has completely atomized, as discussed in Section 5.3. As a result the trend observed in Fig. 6c is one of further broadening of the mass distribution. At the farthest location reported, i.e. $x = 6\,\mathrm{mm}$, the spray has already spread significantly, as shown in Fig. 6d. The asymmetry existing in the near field has resulted in a skewed mass distribution at this location, which is captured fairly well by the computations. We note that there are only 2 computational curves at $x = 6\,\mathrm{mm}$, to reduce computational costs associated with running cases at $\Delta x = 2.8\,\mu\mathrm{m}$ of resolution this far from the near-nozzle region.

4. Linear Stability Analysis – Underlying Assumptions

Most common breakup models are based on the KH framework. The theoretical underpinning of this framework, or of the more general Orr-Sommerfeld (OS) approach, lies in a linearized momentum

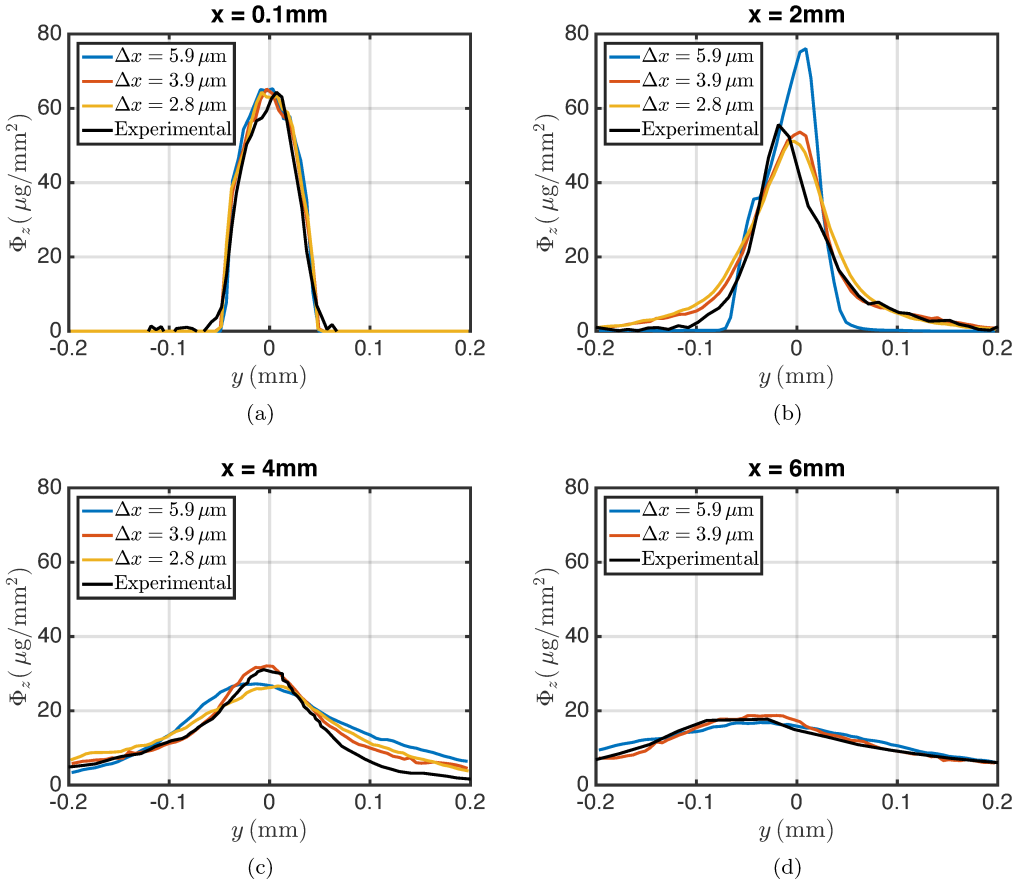

Figure 6: PMD across the jet at four axial locations: (a) $x = 0.1\,\text{mm}$, (b) $x = 2\,\text{mm}$, (c) $x = 4\,\text{mm}$ and (d) $x = 6\,\text{mm}$. The spray axis lies at $y = 0$.

Δx	Centerline		Transverse (Φ_z)			
	Φ_z (Fig. 5a)	Φ_y (Fig. 5b)	x=0.1 mm (Fig. 6a)	x=2 mm (Fig. 6b)	x=4 mm (Fig. 6c)	x=6 mm (Fig. 6d)
5.9 μm	10.7%	7.3%	4.7%	7.7%	5.2%	1.7%
3.9 μm	4.4%	3.5%	3.8%	3.7%	2.5%	1.1%
2.8 μm	2.0%	5.0%	3.9%	4.6%	4.0%	-

Table 3: Relative error values for the PMD curves in Fig. 5 and Fig. 6 computed according to Eq. (10). Although uncertainty in the experimental data used here has not been reported [33, 36] , Kastengren et al. [37] report a standard deviation of up to 4% in their PMD measurements for similar measurements.

equation. The most obvious departure from this treatment is the presence of the non-linear advection term. But in fact, there are more subtle implications of the KH or OS framework that also merit investigation. To see this more clearly we perform the typical base field (upper case) and perturbation

field (lower case) decomposition [38]. For velocity we have

$$\tilde{\mathbf{U}}^q(\mathbf{x},t) = \mathbf{U}^q(\mathbf{x}) + \mathbf{u}^q(\mathbf{x},t), \tag{11}$$

and for pressure

$$\tilde{P}^q(\mathbf{x},t) = P^q(\mathbf{x}) + p^q(\mathbf{x},t), \tag{12}$$

where $(\tilde{\mathbf{U}}, \tilde{P})$ denote the instantaneous velocity and pressure fields, ν is the kinematic viscosity, and the superscript q denotes either the liquid (L) or gas phase (G); $\mathbf{U} = (U, V, W)$; and $\mathbf{u} = (u, v, w)$. Furthermore, the velocity fields can be rewritten in terms of axial terms, along the x coordinate, and a non-axial component or orthogonal component, i.e. $\mathbf{u} = \mathbf{u}_\perp + u\mathbf{e}_x$, and $\mathbf{U} = \mathbf{U}_\perp + U\mathbf{e}_x$ ($\mathbf{e}_x$ is the unit vector in the x-direction).

Substituting the previous decomposition into the incompressible form of the Navier-Stokes equation and recognizing that the base flow field automatically satisfies this equation yields an expression for the perturbed fields

$$\frac{\partial \mathbf{u}^q}{\partial t} + \underbrace{U^q\partial_x\mathbf{u}^q + \mathbf{u}^q_\perp \cdot \nabla \mathbf{U}^q}_{\substack{\text{advection terms present} \\ \text{in the convential system}}} + \underbrace{\overbrace{\mathbf{u}^q \cdot \nabla \mathbf{u}^q}^{\substack{\text{Non-Linear} \\ \text{Perturbation}}} + \overbrace{\mathbf{U}^q_\perp \cdot \nabla \mathbf{u}^q}^{\substack{\text{Non-Axial} \\ \text{Velocity} \\ \text{(Eq. (16))}}} + \overbrace{u^q\partial_x\mathbf{U}^q}^{\substack{\text{Axially Developing} \\ \text{Velocity} \\ \text{(Eq. (18))}}}}_{\text{advection terms ignored in the conventional system}} = -\frac{1}{\rho^q}\nabla p^q + \nu^q\nabla^2\mathbf{u}^q. \tag{13}$$

This expression represents the full form of the governing equation for $(\mathbf{u}^q, p^q)$. In the governing equation commonly seen in linear-stability analyses [38, 39] many of the above terms are ignored (as indicated in Eq. (13)) resulting in the following reduced or conventional form for the PDE governing the perturbed fields

$$\frac{\partial \mathbf{u}^q}{\partial t} + U^q\partial_x\mathbf{u}^q + \mathbf{u}^q_\perp \cdot \nabla \mathbf{U}^q = -\frac{1}{\rho^q}\nabla p^q + \nu^q\nabla^2\mathbf{u}^q. \tag{14}$$

Elaborating on the omitted terms from Eq. (13) as well as other assumptions employed in linear-stability analysis, we have the following:

A. **Non-linear advection**: The velocity perturbations are assumed to be small compared to the base velocity ($\mathcal{O}(u^q) \ll \mathcal{O}(U^q)$). Therefore, the non-linear perturbation terms are ignored.

This is quantified in the present work with the following metric

$$\beta_{NL}(\mathbf{x},t) = \frac{|\mathbf{u}^q \cdot \nabla \mathbf{u}^q|}{|U^q \partial_x \mathbf{u}^q + \mathbf{u}^q_\perp \cdot \nabla \mathbf{U}^q|}. \tag{15}$$

B. **Base velocity**: In the conventional interface instability analysis, the base velocity is assumed to be of the form $\mathbf{U}^q(\mathbf{x}) = U^q(y)\mathbf{e}_x$. This implies that:

i. Non-axial components of the base velocity are zero, i.e. $V^q = W^q = 0$. Therefore, the following part of the advection terms reduces to

$$V^q \frac{\partial \mathbf{u}^q}{\partial y} + W^q \frac{\partial \mathbf{u}^q}{\partial z} = \mathbf{U}^q_\perp \cdot \nabla \mathbf{u}^q = \mathbf{0}. \tag{16}$$

To quantify how well these terms remain at zero the following metric is employed:

$$\beta_{NA}(\mathbf{x},t) = \frac{|\mathbf{U}^q_\perp \cdot \nabla \mathbf{u}^q|}{|U^q \partial_x \mathbf{u}^q + \mathbf{u}^q_\perp \cdot \nabla \mathbf{U}^q|}. \tag{17}$$

ii. Similarly, $\mathbf{U}^q(\mathbf{x})$ is assumed to be fully developed along the jet axis ($\mathbf{U}^q(\mathbf{x}) = \mathbf{U}^q(y,z)$). This implies that,

$$u^q \frac{\partial \mathbf{U}^q}{\partial x} = \mathbf{0}. \tag{18}$$

This assumption is also tested with

$$\beta_{NFD}(\mathbf{x},t) = \frac{|u^q \partial_x \mathbf{U}^q|}{|U^q \partial_x \mathbf{u}^q + \mathbf{u}^q_\perp \cdot \nabla \mathbf{U}^q|}. \tag{19}$$

C. **Interface shape**: For linear stability analysis, the interface is assumed to be described by the superposition of various modes having the following form [3]

$$\xi(x,t) = \sum_{k=-\infty}^{\infty} \xi_k \exp(\omega t + ikx). \tag{20}$$

This appearance is tested by inspection.

To evaluate the metrics defined above, $\mathbf{u}^q$ and $\mathbf{U}^q$ are required. Noting from Eq. (11) that the $\tilde{\mathbf{U}}^q(\mathbf{x},t)$ field can be decomposed as

$$\tilde{\mathbf{U}}^q(\mathbf{x},t) = \mathbf{U}^q(\mathbf{x}) + \mathbf{u}^q(\mathbf{x},t), \tag{21}$$

we perform an averaging operation, $\langle \dots \rangle$, to yield

$$\mathbf{U}^q(\mathbf{x}) = \langle \tilde{\mathbf{U}}^q(\mathbf{x}, t) \rangle. \tag{22}$$

This expression along with Eq. (21) allows us to write

$$\mathbf{u}^q(\mathbf{x}, t) = \tilde{\mathbf{U}}^q(\mathbf{x}, t) - \langle \tilde{\mathbf{U}}^q(\mathbf{x}, t) \rangle. \tag{23}$$

Together Eq. (15) through Eq. (19) provide for a pointwise determination of β_{NL}, β_{NA}, and β_{NFD}. To obtain a more global metric, these quantities are integrated and averaged over a cross-sectional slice of the jet, namely,

$$\overline{\beta_{NL}}(x, t) = \frac{1}{|\Omega^q_\beta|} \iint\limits_{\Omega^q_\beta} \beta_{NL}(\mathbf{x}, t)\, \mathrm{d}y\mathrm{d}z, \tag{24a}$$

$$\overline{\beta_{NA}}(x, t) = \frac{1}{|\Omega^q_\beta|} \iint\limits_{\Omega^q_\beta} \beta_{NA}(\mathbf{x}, t)\, \mathrm{d}y\mathrm{d}z, \tag{24b}$$

$$\overline{\beta_{NFD}}(x, t) = \frac{1}{|\Omega^q_\beta|} \iint_{\Omega^q_\beta} \beta_{NFD}(\mathbf{x}, t) \mathrm{d}y\mathrm{d}z, \tag{24c}$$

where again $q = [L, G]$. The region Ω^L_β is a subset of the y-z plane that extends $3\Delta x$ into the liquid phase from the $\alpha = 0.5$ isoline. Analogously, the Ω^G_β also resides in y-z plane and extends $3\Delta x$ into the gas phase from the $\alpha = 0.5$ isoline. For the internal nozzle domain, Ω^L_β extends three cells from the wall.

Additionally, the metrics are time-averaged as,

$$\langle \overline{\beta_{NL}} \rangle(x) = \frac{1}{t_f - t_i} \int_{t_i}^{t_f} \overline{\beta_{NL}}(x, t)\, \mathrm{d}t, \tag{25a}$$

$$\langle \overline{\beta_{NA}} \rangle(x) = \frac{1}{t_f - t_i} \int_{t_i}^{t_f} \overline{\beta_{NA}}(x, t)\, \mathrm{d}t, \tag{25b}$$

$$\langle \overline{\beta_{NFD}} \rangle(x) = \frac{1}{t_f - t_i} \int_{t_i}^{t_f} \overline{\beta_{NFD}}(x, t)\, \mathrm{d}t, \tag{25c}$$

where t_f and t_i have the same values given in Section 3, namely $t_i = 25\,\mu$s and $t_f = 50\,\mu$s.

5. Results

In the results presented in the following subsections, the quasi-steady or statistically stationary portion of the injection event is exclusively considered. At the corresponding injection speeds considered in the present study, the initial transient period occupies a small fraction of the total injection duration. Also, the phenomena targetted for investigation occur within $x/d_0 \lesssim 50$.

5.1. Examining the Extent of Linear Theory Assumptions

We consider first the behavior of the underlying linear components of advection. These are presented as a function distance from the orifice exit in Fig. 7 both inside the nozzle ($x < 0$) and outside the nozzle ($x > 0$) for the different grid resolution cases. Similar to the validation data presented in Section 3, results for $\Delta x = 5.9\,\mu$m are under-resolved and do not capture the dynamics recorded at the finer grid resolutions. Hence, we focus our discussions on the two finer cases ($\Delta x = 3.9\,\mu$m and $2.8\,\mu$m) for the evaluation of linear advection terms, β_{NL}, β_{NA}, and β_{NFD}. Due to the development of instabilities produced by the growing shear layer, the advection term is significantly affected. It shows an exponential dependence that is given by $U^q\partial_x\mathbf{u}^q + \mathbf{u}^q_\perp \cdot \nabla\mathbf{U}^q \cong C_1 e^{m(x/d_0)}$, where C_1 is a constant and $m = 0.89$ for the finest grid.

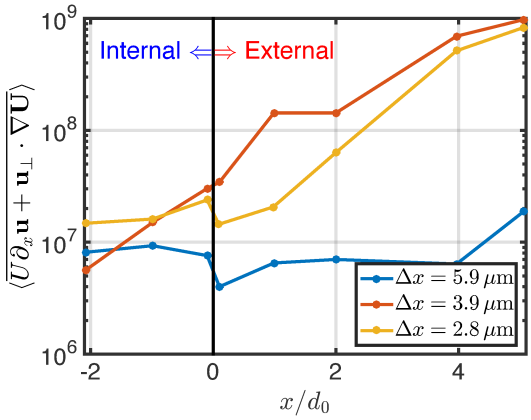

Figure 7: Magnitude of the advection terms in the linearized equation, $U\partial_x\mathbf{u} + \mathbf{u}_\perp \cdot \nabla\mathbf{U}$, corresponding to the liquid phase.

With respect to growth of the non-linear term, Fig. 8 shows the axial profile of β_{NL} (Eq. (15)) in both the liquid (Fig. 8a) and gas (Fig. 8b) phase. For the liquid phase, inside the nozzle ($x < 0$) the terms are $\mathcal{O}(10^{-2})$ and thus the advection is dominated by the linear components. In the external domain ($x > 0$), the relative magnitudes rapidly rise to $\mathcal{O}(10^{-1})$ by $x = 4d_0$. As the grid

size is reduced, the trends show convergence. A similar behavior, but with higher magnitudes, is observed in the gas phase. This indicates that the linearity assumption becomes questionable beyond $x = 4d_0$. It will be shown in Section 5.1.1, that in the vicinity of this region, the associated growth of non-linearities is combined with the development of non-sinusoidal free surface disturbances.

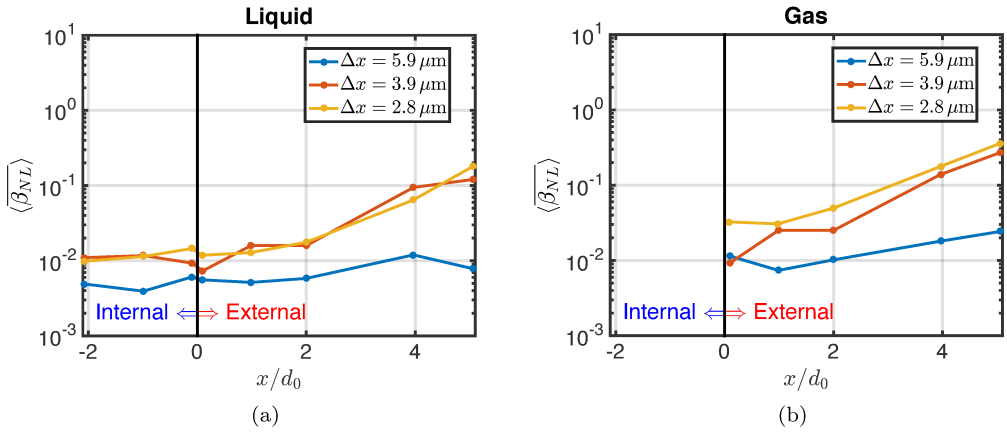

Figure 8: Magnitude of non-linear perturbation in the (a) liquid phase and (b) gas phase.

The trends of the non-axial velocity terms quantified by β_{NA} are shown in Fig. 9 for the liquid and gas phases. Inside the nozzle β_{NA} is $\mathcal{O}(10^{-1})$ indicating that there is a notable non-axial component to the base velocity. This non-axial velocity component is attributed directly to the nozzle imperfections and asymmetries. At the orifice opening the β_{NA} field is large enough that ignoring its presence in linear stability analysis is questionable. Non-axial base velocity at the orifice leads to an asymmetric free surface disturbance, which consequently affects the spray formation. For the gas phase, the magnitude of β_{NA} (Fig. 9b) is higher than that of the liquid phase. β_{NA} remains relatively small through the near-field indicating that non-axial terms are secondary to the dominant growth of the non-linear terms.

Lastly, the results concerning the non-fully developed terms measured by β_{NFD} are shown in Fig. 10 for both liquid and gas phases. At the orifice opening β_{NFD} is around $\mathcal{O}(10^{-1})$, especially for the gas phase (Fig. 10b). The axial gradient discontinuity at $x = 0$ (at the orifice) can be attributed to velocity profile relaxation. This relaxation is produced by a change from a no-slip to a slip boundary condition corresponding to a change from an internal wall-bounded flow to a free surface flow as the fluid travels out of the nozzle.

Downstream from the orifice opening β_{NFD} appears to decrease to $\mathcal{O}(10^{-2})$ for both liquid

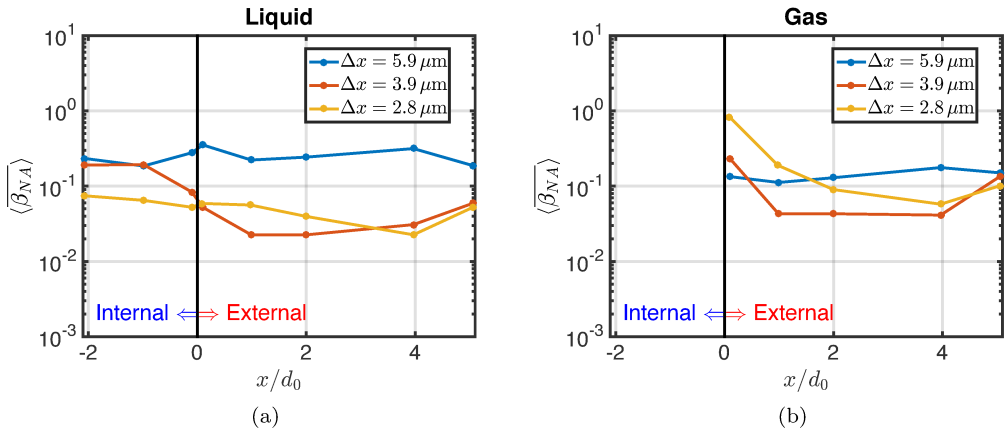

Figure 9: Magnitude of non-axial velocity terms in the (a) liquid phase and (b) gas phase.

and gas phases. Similar to the non-axial terms, the axially developing terms are high enough at the orifice opening that ignoring them is questionable. This behavior is caused by significant gas entrainment in the near orifice region ($x < 2d_0$). Entrainment leads to non-zero gas velocities and velocity gradients. This is seen in the high magnitudes of the non-axial velocity terms, $\mathbf{U}_{\perp}^{(g)} \cdot \nabla \mathbf{u}^{(g)}$, and axially developing velocity terms, $u^{(g)} \partial_x \mathbf{U}^{(g)}$, in Fig. 9b and Fig. 10b, respectively. Beyond the immediate nozzle region, the magnitudes of β_{NFD} quickly relax to much lower values $\sim \mathcal{O}(10^{-2})$ indicating that from a linearly stability analysis perspective they can be neglected to a reasonable approximation. It is actually the non-linear term, which grows quickly and is *primarily responsible for invalidating* the assumptions employed in the stability analysis.

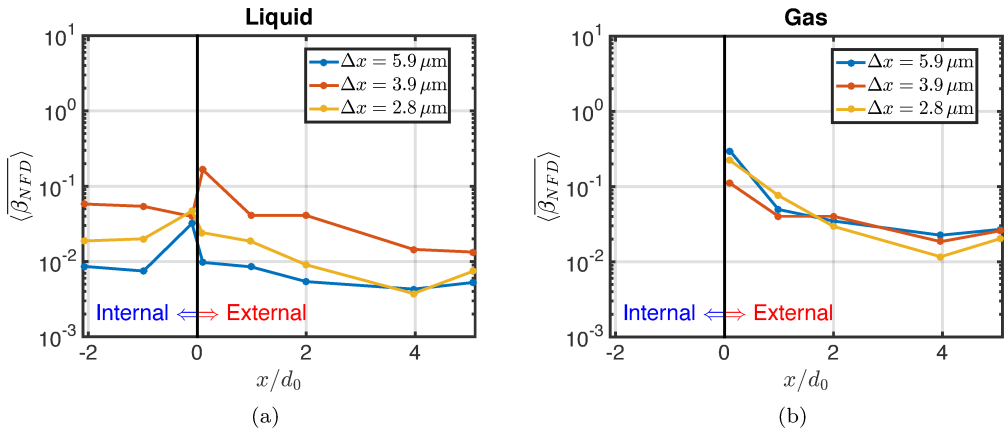

Figure 10: Magnitude of axially-developing term in the (a) liquid phase and (b) gas phase.

5.1.1. Surface Disturbances

The conventional view of the spray formation process embodied in spray models [12–19] consists of a liquid, which is initially perturbed by a multitude of infinitesimal axisymmetric perturbations, and where the fastest growing mode (governed by linear stability analysis) emerges to dominate the disturbances. This fastest and most violent mode grows beyond the initial sinusoidal characterization and is then responsible for the breakup of the liquid jet, i.e. it produces primary atomization. It is tacitly assumed that during this process of surface growth from sinusoidal to highly erratic surface shape, the underlying flow field is similarly undergoing a transition into the full non-linear regime.

We contrast this view by observing the results of simulations as depicted in Fig. 11 over four different axial orientations. Over a distance of approximately 5 diameters from the orifice, the surface disturbances are highly irregular with strong asymmetries, which are far from the expected axisymmetric normal mode [20]. However, the magnitude of these disturbances is significantly smaller than the jet diameter, and most of them are still single value functions of the radial coordinate (the interface has not folded over itself).

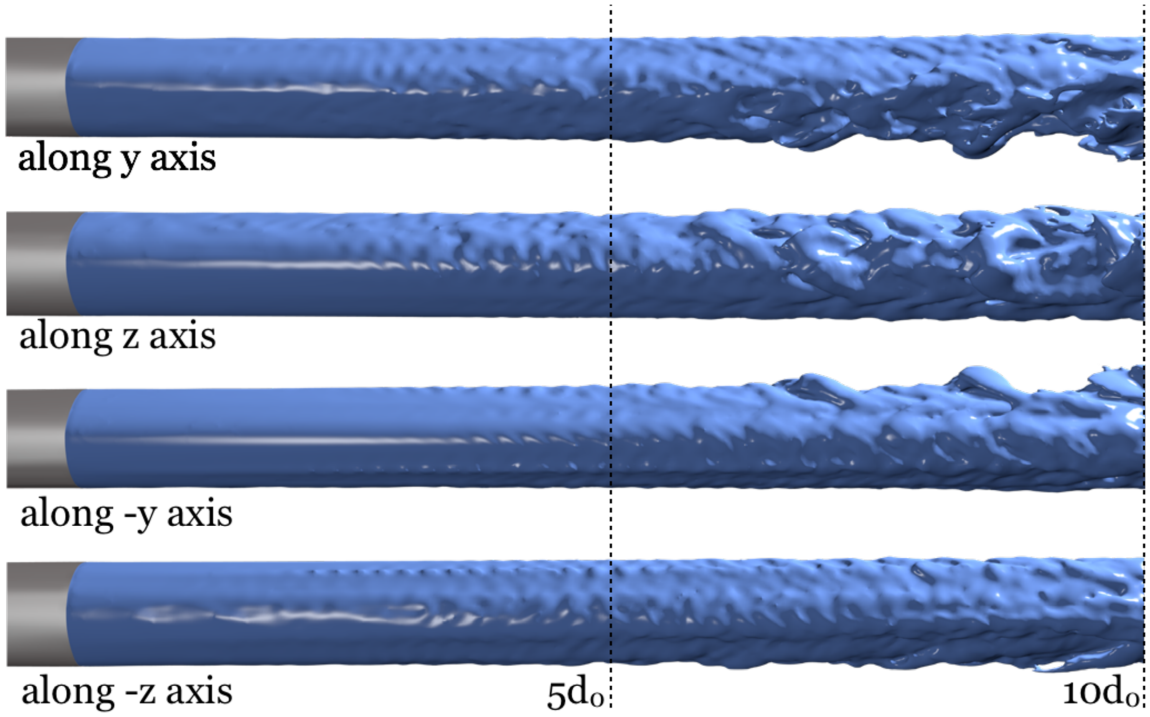

Figure 11: Near field (up to $x = 10d_0$) jet surface morphology from four different viewing orientations. A view along the y axis is shown at the top followed by three other views (sequential rotations of 90° about the x axis).

In the work of McCarthy and Molloy [40], it is discussed that as the flow exits the nozzle,

thereby losing the wall constraint, turbulent lateral motion of the fluid leads to surface disturbances. In addition to the loss of the wall constraint, complex flow development inside the nozzle due to surface irregularities and non-symmetrical orifice shape are likely to blame for the observed level of interface irregularity. These near-nozzle irregularities have also been reported in recent experimental visualization as well [41–43]. The images in Fig. 11 reveal that the surface is characterized by the presence of disturbance streaks aligned along the streamwise direction. And that slightly beyond $x/d_0 = 5.5$, the surface shows signs of developing lobes, which force the surface to fold over itself and become a multivalued function of the radial coordinate.

To visualize more clearly the evolving complexity of free surface disturbance within the range $4.5 < x/d_0 < 8$ in a cross-sectional x-y plane containing the centerline, the instantaneous free surface is compared to a Fourier fit (8 modes) in Fig. 12. While the surface remains a single value function of r at $x/d_0 < 5.5$, it distinctly loses this quality at $x/d_0 \approx 7.7$. Similar lobe structures have also been identified in the liquid jet and liquid sheet simulation work of Sirignano and co-workers [44, 45]. At $x/d_0 \simeq 5$, Section 5.1 has already established that the non-linearities have developed beyond 10% of its linear counterpart. We see that this departure coincides with a significant level of surface deformation, which is far more complex than the axi-symmetrical disturbances predicted by linear theory.

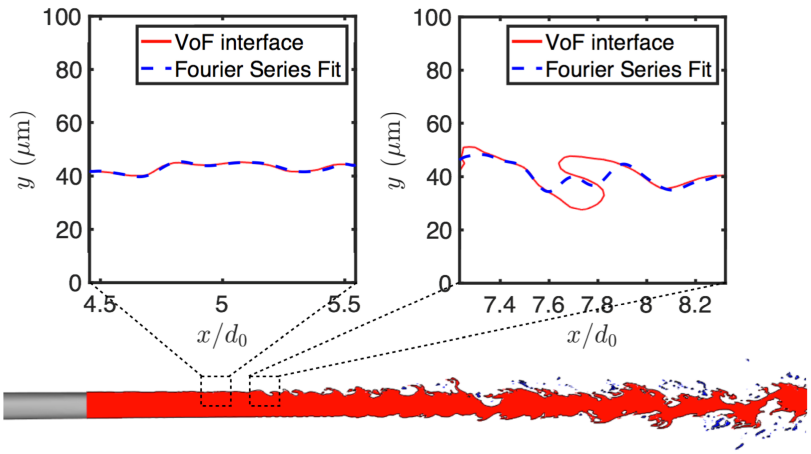

Figure 12: A cross sectional view of the near field is presented at the bottom. The two insets display the VoF interface at two axial locations along with a Fourier series fit (8 modes) through the interface data suggested by the mathematical form given in Eq. (20). In the first inset the wave amplitudes are small and the interface can be represented well by a sum of sinusoidal modes. As we move downstream the interface is no longer represented by a single-valued function of r.

5.2. Comparison between VoF and Linear Stability

Close to the injector orifice, specifically for $x/d_0 \leq 5$, the non-linearities are small enough that a comparison can be made between the VoF simulation results and those stemming from a linear stability analysis. It should be kept in mind that the complexity of the flow emanating from the nozzle after its passage through its interior is significantly more complex from the standard base flow fields presented in texts [38, 39] and subsequently analyzed via the Orr-Sommerfeld equation. Hence, we should not expect to arrive at a perfectly consistent comparison; nevertheless, for the sake of estimating the associated dominant wavelengths, it is instructive to perform this investigation.

The two-phase Orr-Sommerfeld solution is computed from a previously published procedure by Deshpande et al. [10], where all dynamic and kinematic interfacial conditions are enforced. Additionally, the base liquid and gas phase boundary layers are obtained from the current simulations. To allow for uncertainties between these boundary layer thickness values, different variations are considered, and the corresponding wavelengths for the most violent modes are presented in Table 4.

		δ_L		
		7 μm	10 μm	15 μm
δ_G	7 μm	40.8 μm	57.1 μm	81.6 μm
	10 μm	40.8 μm	58.3 μm	81.6 μm
	15 μm	40.8 μm	58.3 μm	87.4 μm

Table 4: Wavelenghts of most unstable modes from OS calculations.

To estimate the wavelengths of the surface disturbances from the VoF simulations, various probes are placed within $4 < x/d_0 < 5$. As seen in Fig. 11 and documented in Section 5.1, this region of the domain places the surface disturbances well within the linear regime. Time history of the interface perturbation is presented in Fig. 13. The interface perturbation, denoted as $\xi(x = 4d_0, z = 0)$ for instance, is the distance of the interface from its unperturbed location, $(x = 4d_0,\ y = 45\,\mu m,\ z = 0)$. Similarly, $\xi(x = 4d_0, y = 0)$ is the distance of the interface from its unperturbed location, $(x = 4d_0,\ y = 0,\ z = 45\,\mu m)$.

The $\xi(x, z = 0, t)$ and $\xi(x, y = 0, t)$ data is then analyzed in the frequency domain through a Fast Fourier Transform. The underlying flow field predictions from VoF are interrogated revealing that the surface disturbances are traveling at $U_\xi = 412$ ms^{-1}, and this velocity is largely constant in time. Therefore, the wavelengths associated with the frequencies are obtained as $\lambda = U_\xi/f$. The resulting wavelength spectra for the data is presented in Fig. 14. It is observed that the most dominant

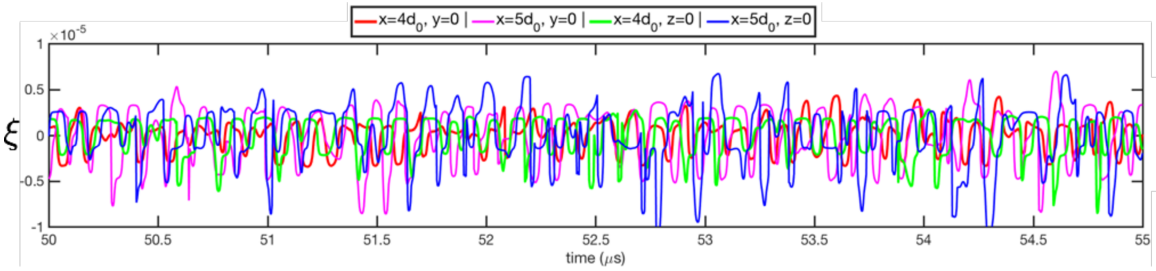

Figure 13: Interface perturbation, ξ, is presented as a function of time in the x-y plane and x-z plane, at two axial locations, $x = 4d_0$ and $x = 5d_0$.

modes, defined here as the modes with amplitudes within 20% of the maximum amplitude, are in the range of $\lambda = 40.4\,\mu$m to $\lambda = 71.0\,\mu$m.

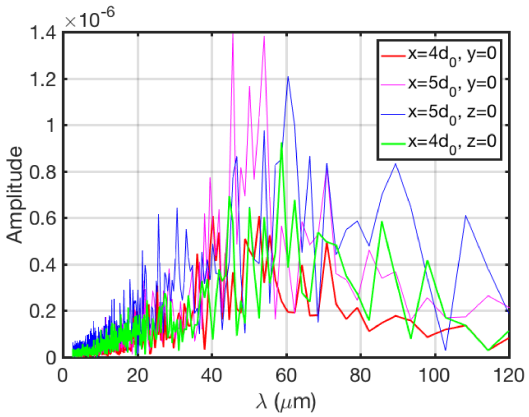

Figure 14: Frequency spectra for interface elevation data from $z = 0$ plane and $y = 0$ plane.

The Orr-Sommerfeld growth spectra, obtained as described in [10], are shown in Fig. 15. Dominant modes from the VoF simulations are overlaid on the plot as a band. The fastest growing modes from the OS calculation are in the range of $40.8\,\mu$m to $87.4\,\mu$m, and those from the VoF simulations are in the range of $40.4\,\mu$m to $71.0\,\mu$m. A strong overlap between the OS prediction and the simulation data indicates that linear stability theory predicts relatively well the wavelengths of the most unstable modes in a realistic liquid injection setup.

5.3. Implications for Primary Atomization

To provide an insightful perspective of the internal structure of the liquid jet, various cross-sectional views of liquid fraction field (α) are displayed in Fig. 16. Each of these views corresponds to a plane that intersects the jet centerline. The images reveal that while the surface of the jet begins to display breakup at $x/d_0 \approx 7$, the underlying liquid core remains intact. Due to the asymmetric

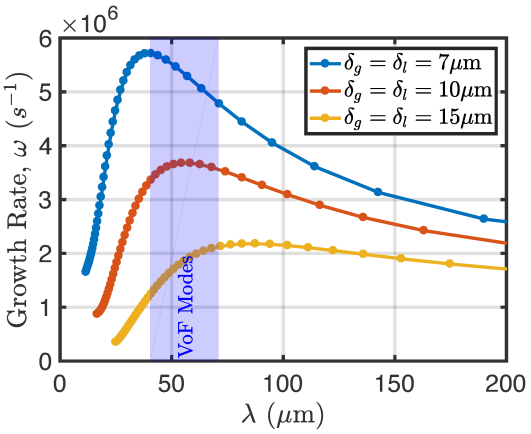

Figure 15: Orr-Sommerfeld growth spectra for 3 different velocity profiles, where δ_G and δ_L represent the gas and liquid boundary layer thicknesses, respectively. From Table 4, the O-S predicts that the most unstable modes lie between 40.8 μm to 87.4 μm. The most unstable modes detected in the VoF simulations lie in the region highlighted in blue.

flow emanating from the nozzle, the level of surface disintegration is not uniform along the azimuthal coordinate with some sections of the jet showing more vigorous breakup than other sections at the same axial location. However, by $x/d_0 \approx$ 8, the surface is already breaking up all around the jet. This relatively near nozzle location for breakup is much closer than the location where the entire jet breakups, or by definition the location of primary atomization. Fig. 17 presents a time history of the length of the intact liquid core, which provides instantaneous information of the primary atomization region. It lies approximately between $x/d_0 = 30$ and $x/d_0 = 40$, with a mean value of $\overline{x/d_0} = 37.8$ diameters.

The fact that the flow has become highly non-linear and that the surface of the jet undergoes breakup relatively close to the nozzle is in contrast with the fact that the liquid core remains intact until much further downstream. This observation calls to question the conventional view of the atomization process [2–4], inherited widely in spray models, where the most unstable mode predicted by linear stability analysis is viewed as the responsible agent for completely fragmenting the liquid jet.

The current simulations and analysis show that the most unstable modes do exist under the present conditions, but that their action is limited to the breakup of the surface of the jet, not in cutting it off completely. Hence, *they are not directly associated with primary atomization.* This is also in agreement with previous observations presented for the case of an injected liquid sheet [10], where it was reported that the most unstable OS modes have length scales that are two to three

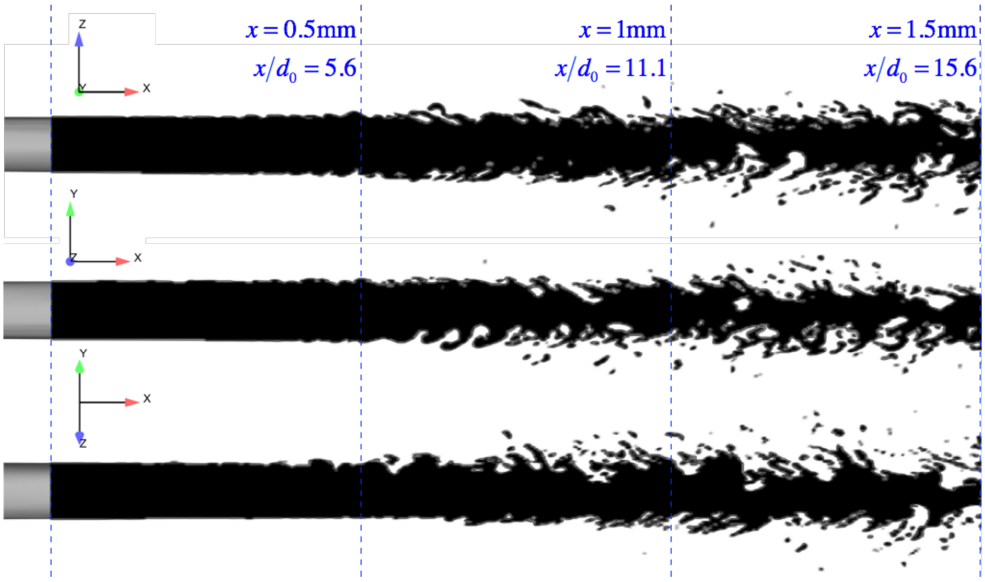

Figure 16: Computational images of the near-field jet breakup corresponding to orientations along the y-axis, z-axis, and midpoint point axis between the z and y axes. The images show surface breakup beginning at $x/d_0 \approx 7$.

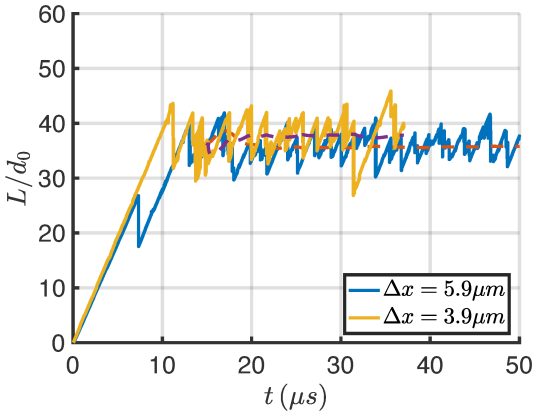

Figure 17: Time history of the intact core length, defined as the maximum liquid length that is topologically connected to the orifice. The mean $\overline{L}/d_0 = 37.8$, and the standard deviation, $\sqrt{\overline{[(L/d_0) - \overline{L}/d_0]^2}} = 3.2$.

orders of magnitude smaller than the sheet thickness and are thus responsible for atomizing the surface of the sheet, but not the sheet itself. Similar findings have been reported by Marmottant and Villermaux [46], albeit under significantly different configurations. Marmottant and Villermaux employed a coaxial jet arrangement and reported an initial instability followed by a secondary one responsible for primary atomization. Fig. 18 presents an illustration of the process.

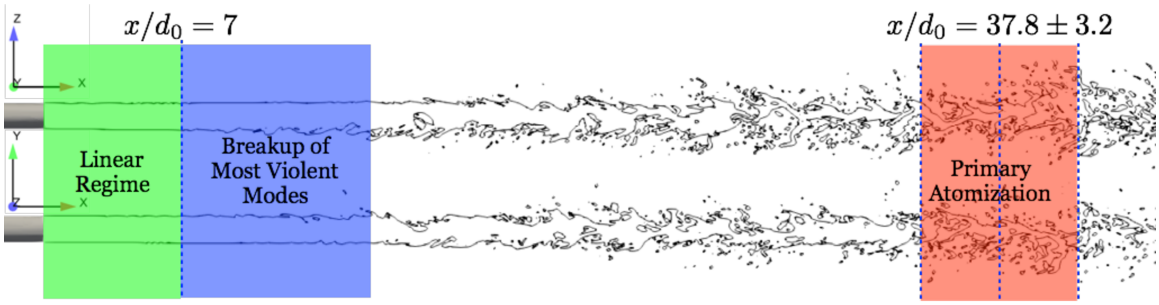

Figure 18: Two instantaneous images of the jet breakup, with viewing directions oriented along the y and the z axis, are presented here. The image highlights 3 distinct parts of the atomization process. Linear modes of the surface disturbances exist initially up to $x/d_0 = 7$. Further downstream, the dominant modes grow and breakup the surface, but the liquid core remains unpreturbed. Finally primary atomization, or the complete destruction of the liquid core is observed around $x/d_0 = 37.8$.

6. Conclusions

After successfully comparing high-resolution simulation data to recent X-ray radiography measurements [33, 36], the extent of the linearity treatment and accompanying assumptions in spray models is investigated. It is found that non-axial flow and non-fully developed conditions are present right at the orifice location, but that these do not show signs of significant growth (exponential). It is actually, the non-linear flow development that exhibits the greatest and sustained growth, where it is shown that at 4 diameters downstream, it is already approximately 10% of the linear advection part. Similarly, the conventionally assumed sinusoidal surface disturbances are largely absent, and the surface of the jet is irregularly distorted right from the start of the external domain. These disturbances lead to interface folding over itself at $x/d_0 \approx 7$ and subsequent formation of small ligaments and drops. Due to the real flow conditions emanating from the orifice, as opposed to idealistic conditions of steady and spatially uniform flow, these characteristics are expected.

Comparing the wavelength of the most unstable modes between the OS linear stability predictions and VoF simulations, the results show reasonably agreement being mindful of the fact that the real base flow field is not the same as the conventional one adopted in OS analysis. Even though these initial disturbance modes are clearly the most unstable, they are not sufficiently large to completely rupture the jet. Their impact is limited to stripping off the surface of the liquid jet, while the jet core remains unperturbed. This surface stripping is found to start somewhere between $x/d_0 = 7$ and $x/d_0 = 10$, whereas the jet core undergoes complete atomization at a mean value of $x/d_0 = 37.8$, i.e. approximately 30 diameters downstream. A subsequent mode develops once the flow has become fully-nonlinear, and it is this more violent process that leads to primary atomization. Similar

observations have been reported in the literature for liquid sheet undergoing atomization [10] and for a liquid jet in a co-axial configuration exposed to a fast moving air stream [46].

A key outcome from this work questions the validity of the common spray model assumptions linking linear stability with primary atomization, at least for realistic cases such as the present one using Spray A. A related question centers on the level of agreement typically reported between spray model predictions and experiments concerning liquid penetration vs. time. This level of error is usually well below 5%, which would tend to confirm the applicability of linear stability theory. However, it should be kept in mind that the practical application of this theory is combined with the introduction of a good number of modeling constants [4], and that these constants have been fined-tuned over the years to match experimental data. Thus, the level of agreement reported is not really a validation of linear-stability-theory based models, but rather a confirmation that the constants have been appropriately optimized.

Similar conclusions questioning the validity of the linear stability rooted in the KH analysis and its adoption into breakup models have recently been presented by Kastengren et al. [41]. Their reasoning revolved around the absence of nano-scale droplet population in their measurements, which is predicted by KH. This extremely small droplet size distribution emanates from an infinitely sharp boundary layer at the interface, i.e. a discontinuous velocity field. In fact, predictions from the more general OS [10], which includes viscosity effects, reveal that as the boundary layer is thickened the length scale of the most unstable mode, and the associated droplets emanating from them, grow noticeably in size. Hence, we can have droplets of much larger size than the KH generated nano-droplets, but the dynamics can still be completely governed by the breakup of the most unstable modes of linear stability theory. What the present work suggests is that even these larger scales disturbances predicted by linear stability theory do not fracture the liquid core. Their influence is restricted to the surface.

7. Acknowledgements

This material is based on work supported by the Direct-Injection Engine Research Consortium (DERC) at UW-Madison and the National Science Foundation through Ronald Joslin, Fluid Dynamics Program Director (Award #1703825). The authors would like to thank the Engine Combustion Network for providing injector geometry files and other resources. Our thanks are also due to Center for High Throughput Computing (CHTC) at UW-Madison for providing computing resources,

along with Joshua Leach for administering the computing resources within the research group. CEI is acknowledged for granting use of their post-processing software, EnSight, during the early phase of the work.

8. References

[1] M. Gorokhovski, M. Herrmann, Modeling primary atomization, Annu. Rev. Fluid Mech. 40 (2008) 343–366.

[2] A. H. Lefebvre, V. G. McDonell, Atomization and Sprays, CRC press, 2017.

[3] S. Lin, R. Reitz, Drop and spray formation from a liquid jet, Annual Review of Fluid Mechanics 30 (1) (1998) 85–105.

[4] R. Reitz, L. Pickett, M. Trujillo, Fuel introduction, Encyclopedia of Automotive Engineering.

[5] R. Lebas, T. Menard, P.-A. Beau, A. Berlemont, F.-X. Demoulin, Numerical simulation of primary break-up and atomization: Dns and modelling study, International Journal of Multiphase Flow 35 (3) (2009) 247–260.

[6] J. Shinjo, A. Umemura, Simulation of liquid jet primary breakup: dynamics of ligament and droplet formation, International Journal of Multiphase Flow 36 (7) (2010) 513–532.

[7] J. Shinjo, A. Umemura, Surface instability and primary atomization characteristics of straight liquid jet sprays, International Journal of Multiphase Flow 37 (10) (2011) 1294–1304.

[8] J. Shinjo, A. Umemura, Detailed simulation of primary atomization mechanisms in diesel jet sprays (isolated identification of liquid jet tip effects), Proceedings of the Combustion Institute 33 (2) (2011) 2089–2097.

[9] M. Arienti, M. Sussman, An embedded level set method for sharp-interface multiphase simulations of diesel injectors, International Journal of Multiphase Flow 59 (2014) 1–14.

[10] S. S. Deshpande, S. R. Gurjar, M. F. Trujillo, A computational study of an atomizing liquid sheet, Physics of Fluids 27 (8) (2015) 082108.

[11] D. Jiao, F. Zhang, Q. Du, Z. Niu, K. Jiao, Direct numerical simulation of near nozzle diesel jet evolution with full temporal-spatial turbulence inlet profile, Fuel 207 (2017) 22–32.

[12] F. D. Chuahy, S. L. Kokjohn, Effects of the direct-injected fuel's physical and chemical properties on dual-fuel combustion, Fuel 207 (2017) 729–740.

[13] C. Kavuri, S. L. Kokjohn, Computational optimization of a reactivity controlled compression ignition (RCCI) combustion system considering performance at multiple modes simultaneously, Fuel 207 (2017) 702–718.

[14] H. Wang, R. D. Reitz, M. Yao, B. Yang, Q. Jiao, L. Qiu, Development of an n-heptane-n-butanol-pah mechanism and its application for combustion and soot prediction, Combustion and Flame 160 (3) (2013) 504–519.

[15] B. Yang, M. Yao, W. K. Cheng, Y. Li, Z. Zheng, S. Li, Experimental and numerical study on different dual-fuel combustion modes fuelled with gasoline and diesel, Applied Energy 113 (2014) 722–733.

[16] Z. Chen, Z. Wu, J. Liu, C. Lee, Combustion and emissions characteristics of high n-butanol/diesel ratio blend in a heavy-duty diesel engine and EGR impact, Energy Conversion and Management 78 (2014) 787–795.

[17] N. Abani, S. Kokjohn, S. Park, M. Bergin, A. Munnannur, W. Ning, Y. Sun, R. D. Reitz, An improved spray model for reducing numerical parameter dependencies in diesel engine CFD simulations, Tech. rep., SAE Technical Paper (2008).

[18] S. Som, S. K. Aggarwal, Effects of primary breakup modeling on spray and combustion characteristics of compression ignition engines, Combustion and Flame 157 (6) (2010) 1179–1193.

[19] B. Mohan, W. Yang, S. kiang Chou, Development of an accurate cavitation coupled spray model for diesel engine simulation, Energy Conversion and Management 77 (2014) 269–277.

[20] R. Reitz, Modeling atomization processes in high-pressure vaporizing sprays, Atomisation and Spray Technology 3 (4) (1987) 309–337.

[21] J. C. Beale, R. D. Reitz, Modeling spray atomization with the Kelvin-Helmholtz/Rayleigh-Taylor hybrid model, Atomization and Sprays 9 (6) (1999) 623–650.

[22] Y. D. Shikhmurzaev, Capillary Flows with Forming Interfaces, Chapman and Hall/CRC, 2008.

[23] S. Lin, Breakup of Liquid Sheets and Jets, Cambridge university press, 2003.

[24] D. Fuster, J. Matas, S. Marty, S. Popinet, J. Hoepffner, A. Cartellier, S. Zaleski, Instability regimes in the primary breakup region of planar coflowing sheets, Journal of Fluid Mechanics 736 (2013) 150–176.

[25] R. D. Reitz, F. V. Bracco, Mechanism of breakup of round liquid jets, in: Encyclopedia of Fluid Mechanics, Gulf Publishing Company, 1986, Ch. 10.

[26] S. S. Deshpande, L. Anumolu, M. F. Trujillo, Evaluating the performance of the two-phase flow solver interfoam, Computational Science & Discovery 5 (1) (2012) 014016.

[27] B. Van Leer, Towards the ultimate conservative difference scheme. ii. monotonicity and conservation combined in a second-order scheme, Journal of Computational Physics 14 (4) (1974) 361–370.

[28] Openfoam user guide, the open source CFD toolbox user guide, version 1.5. openCFD limited.

[29] J. Brackbill, D. B. Kothe, C. Zemach, A continuum method for modeling surface tension, Journal of Computational Physics 100 (2) (1992) 335–354.

[30] R. I. Issa, Solution of the implicitly discretised fluid flow equations by operator-splitting, Journal of Computational Physics 62 (1) (1986) 40–65.

[31] M. M. Francois, S. J. Cummins, E. D. Dendy, D. B. Kothe, J. M. Sicilian, M. W. Williams, A balanced-force algorithm for continuous and sharp interfacial surface tension models within a volume tracking framework, Journal of Computational Physics 213 (1) (2006) 141–173.

[32] A. L. Kastengren, F. Z. Tilocco, C. F. Powell, J. Manin, L. M. Pickett, R. Payri, T. Bazyn, Engine combustion network (ECN): measurements of nozzle geometry and hydraulic behavior, Atom. Sprays 22 (12) (2012) 1011–1052.

[33] A. L. Kastengren, F. Z. Tilocco, D. J. Duke, C. F. Powell, X. Zhang, S. Moon, Time-resolved x-ray radiography of sprays from engine combustion network spray a diesel injectors, Atomization and Sprays 24 (3) (2014) 251–272.

[34] R. Payri, J. Gimeno, J. Cuisano, J. Arco, Hydraulic characterization of diesel engine single-hole injectors, Fuel 180 (2016) 357–366.

[35] M. Arienti, M. Sussman, A high-fidelity study of high-pressure diesel injection, in: SAE 2015-01-1853, 2015.

[36] Q. Xue, M. Battistoni, C. Powell, D. Longman, S. Quan, E. Pomraning, P. Senecal, D. Schmidt, S. Som, An eulerian CFD model and x-ray radiography for coupled nozzle flow and spray in internal combustion engines, International Journal of Multiphase Flow 70 (2015) 77–88.

[37] A. Kastengren, C. Powell, T. Riedel, S.-K. Cheong, K.-S. Im, X. Liu, Y. Wang, J. Wang, Nozzle geometry and injection duration effects on diesel sprays measured by x-ray radiography, Journal of Fluids Engineering 130 (4) (2008) 041301.

[38] P. J. Schmid, D. S. Henningson, Stability and transition in shear flows, Vol. 142, Springer Science & Business Media, 2012.

[39] P. G. Drazin, W. H. Reid, Hydrodynamic Stability, Cambridge university press, 2004.

[40] M. McCarthy, N. Molloy, Review of stability of liquid jets and the influence of nozzle design, The Chemical Engineering Journal 7 (1) (1974) 1–20.

[41] A. Kastengren, J. Ilavsky, J. P. Viera, R. Payri, D. Duke, A. Swantek, F. Z. Tilocco, N. Sovis, C. Powell, Measurements of droplet size in shear-driven atomization using ultra-small angle X-ray scattering, International Journal of Multiphase Flow 92 (2017) 131–139.

[42] M. Ghiji, L. Goldsworthy, P. Brandner, V. Garaniya, P. Hield, Analysis of diesel spray dynamics using a compressible Eulerian/VOF/LES model and microscopic shadowgraphy, Fuel 188 (2017) 352–366.

[43] C. Crua, M. R. Heikal, M. R. Gold, Microscopic imaging of the initial stage of diesel spray formation, Fuel 157 (2015) 140–150.

[44] D. Jarrahbashi, W. Sirignano, Vorticity dynamics for transient high-pressure liquid injection, Physics of Fluids 26 (101304) (2014) 1–52.

[45] A. Zandian, W. Sirignano, F. Hussain, Planar liquid jet: Early deformation and atomization cascades, Physics of Fluids 29 (062109) (2017) 1–20.

[46] P. Marmottant, E. Villermaux, On spray formation, Journal of Fluid Mechanics 498 (2004) 73–111.